PREDICTION OF VORTEX SHEDDING FROM FOREBODIES WITH CHINES

Michael R. Mendenhall
Daniel J. Lesieutre

Nielsen Engineering & Research, Inc.
510 Clyde Ave., Mountain View, CA 94043
USA

SUMMARY

An engineering prediction method to calculate vortex shedding from noncircular forebodies with sharp chine edges in subsonic flow at large incidence angles is presented. The forebody is represented by two- and three-dimensional singularities, and the lee side vortex wake is modeled by discrete vortices in crossflow planes along the body. The computational procedure is described, and comparisons of measured and predicted surface pressure distributions and predicted flow field vectors are presented to illustrate the method.

INTRODUCTION

Current flight vehicle applications requiring increased aerodynamic performance can involve a variety of noncircular body shapes in subsonic flow at high angles of attack and nonzero roll angles. When these bodies have sharp edges, chines, or wing leading edge extensions, separation is fixed at the sharp edge, and the lee side vortex wake is different from the wake formed on the lee side of a smooth body. As in the case of smooth bodies, the chine-body vortex shedding characteristics are directly influenced by the body cross-sectional shape and the local flow conditions. It is desirable to model the lee side vortex wake by means of a rational method capable of considering a variety of body shapes over a wide range of incidence angles and Mach numbers. It is important that the nonlinear aerodynamic characteristics of the configuration caused by vortex wake-induced effects be modeled with a method which correctly represents the physical characteristics of the actual flow field. However, for preliminary design and analysis applications, it is also important the method be economical to use.

The flow phenomena of concern are the sheets of vorticity formed when the fluid flow separates from the sharp edges on both sides of the body (Fig. 1). One approach for modeling these distributed vorticity fields has involved the use of clouds of discrete potential vortices. Underlying the basic approach is the analogy between two-dimensional unsteady flow past a body and the steady three-dimensional flow past an inclined body. The three-dimensional steady flow problem can be reduced to the two-dimensional unsteady separated flow problem for solution. Linear theory for the attached flow model and the vortex analogy are combined to produce a nonlinear prediction method.

A method to predict vortex shedding flow phenomena from smooth bodies, both circular and noncircular, in subsonic flow, is described in Refs. 1 and 2. The extension of the prediction method to supersonic flow is described in Ref. 3. Other investigators have used this approach to successfully model the subsonic flow phenomena in the vicinity of circular cross section bodies.[4] Ref. 5 provides a comprehensive review of many of the discrete vortex methods currently available and the inherent problems involved with their use.

The purpose of this paper is to document the extension of the subsonic analysis of Ref. 1 to predict the vortex shedding characteristics of forebodies with sharp corners or chines. A code, VTXCHN, was developed for this purpose.[6] This code is an engineering prediction method which provides a preliminary design and analysis capability with reasonable accuracy and economy.

LIST OF SYMBOLS

A_k	coefficients of conformal transformation
C_p	pressure coefficient
K	total number of Fourier coefficients used to describe transformation
M_∞	free-stream Mach number
r'	radial distance to a point on a noncircular body, Fig. 3
r_{eq}	radius of equivalent circular body
r_o	radius of transformed circle
s	semispan
u,v,w	velocity components in real plane
U	local velocity
V_∞	free-stream velocity
W	complex potential
x,y,z	body coordinate system with origin at the nose: x positive aft along the model axis, y positive to starboard, and z positive up
α	angle of attack
α_c	angle between free-stream velocity vector and body axis
β	angle of sideslip; also polar angle in σ-plane, Fig. 3
β'	local slope of body surface, Fig. 3
Δx	axial interval for marching procedure
γ	ratio of specific heats
Γ	vortex strength
ζ	complex coordinate in an intermediate plane, Fig. 2
ν	complex coordinate in circle plane, Fig. 2
ξ,η	lateral and vertical coordinates in an intermediate plane, Fig. 2
σ	complex coordinate in real plane, Fig. 2
τ,λ	lateral and vertical coordinates in circle plane, Fig. 2
Φ	velocity potential in real plane
Ψ	stream function in real plane

Subscripts and Superscripts

$()_{eq}$	equivalent body
$()_m$	vortex m
$()_{\Delta n}$	perturbation due to noncircular shape
$()'$	incompressible quantity; or surface values in Fig. 3

METHODS OF ANALYSIS

Background

Prediction of vortex shedding from configurations with sharp edges at high angles of attack has been an important research area for a number of years because of the dominating effect of the vortex field on the nonlinear aerodynamics of fighter aircraft and missiles. Most of this work emphasized sharp edged delta wings because of the availability of experimental data. Unfortunately, forebodies with chines have not experienced this same intensity of study; therefore, the knowledge base for this flow phenomena is not as well developed.

A brief examination of the methods and techniques applied to the prediction of vortex shedding from delta wings and wing-bodies at high angles of attack was made to help put the chine problem into perspective. It is not the purpose of this work to review all the theoretical analyses of delta wings; others have already accomplished detailed reviews.[5,7]

An early successful model of the vortex shed from the leading edge of a delta wing is described in Ref. 8. In this model, the feeding sheet from the wing leading edge is a straight vortex sheet ending in a concentrated vortex. The effect of the feeding sheet on the crossflow plane is neglected; however, the results are good for low aspect ratio wings. A more detailed treatment of slender delta wings is presented in Ref. 9. In this method, the effect of the feeding sheet is considered, but a conical flow assumption is required which limits the application to low aspect ratios. A complex vortex model consisting of a cloud of discrete vortices is described in Ref. 10. This model is more flexible in the shape and influence of the feeding sheet and the rolled-up vortex, but as implemented in Ref. 10, it can be used only to calculate the force and center of pressure on thin wings and bodies. This latter approach has a number of features which make it desirable for bodies with chines, and it is very compatible with the smooth body vortex shedding technique.

The next improvement to the vortex cloud approach is the representation of the wing with a panel method as described in Ref. 7. This method has the capability of predicting wing pressure distributions under the influence of the shed vorticity, and it could be extended to more complex configurations. However, a conical flow assumption is part of the method, and it is not clear if the method is applicable to very small wings or chines. Finally, the use of three-dimensional panel methods to represent both the wing and shed vortex have proved to be accurate and applicable to a wide variety of configurations.[11,12] These methods require an iterative calculation procedure to converge on the proper vortex strength and position, which can cause the run times to be excessive in many cases.

The next level of complexity beyond the methods discussed above involves solutions of the Euler and Navier-Stokes equations. There is no doubt that the state of the art in computational fluid dynamics is changing dramatically at this time, and the capability of handling the forebody with chine is available for research purposes. However, for preliminary design analysis, the CFD methods are still much too expensive and difficult to use.

General Approach

The calculation procedure for chined forebodies is carried out in a manner similar to that for smooth bodies described in detail in Ref. 1. The volume of an equivalent axisymmetric body is represented by discrete point sources and sinks and doublets, and the strengths of the individual singularities are determined to satisfy a flow tangency condition on the body in a nonseparated uniform flow at angles of incidence and roll. Compressibility effects on the body are included by a Gothert transformation which keeps the cross section shape unchanged but stretches the axial body coordinate. This compressibility correction is valid up to Mach numbers where local shock waves develop. Starting at a crossflow plane near the body nose, the pressure distribution on the body is computed using the full compressible Bernoulli equation. The body shape determines the location of separation as the assumption is made that separation occurs at the sharp edge, and the shed vorticity originates at that point.

At the separation points, incompressible vortices with their strengths and positions determined by the requirement that the Kutta condition at the sharp edge be satisfied are shed into the flow field. The trajectories of these free vortices between this crossflow plane and the next plane downstream are calculated by integration of the equations of motion of each vortex, including the influence of the free stream, the body, and other vortices. The pressure and trajectory calculations are carried out by mapping the noncircular cross section shape to a circle using numerical conformal transformations. Image vortices are required inside the circle to satisfy the flow tangency boundary condition on the body cross section.

At the next downstream crossflow plane, new vortices are shed, adding to the vortex feeding sheet and cloud representing the wake on the lee side of the body. This procedure is carried out in a stepwise fashion over the length of the forebody.

The development of an engineering method to predict the pressure distributions on arbitrary missile or aircraft forebodies in subsonic flow at high angles of incidence requires the use of a number of individual prediction techniques. In the remainder of this section, the individual methods are described briefly, and the section concludes with a description of the complete calculation procedure. Since many of these individual methods have been described previously, they will be included by reference.

Conformal Mapping

The crossflow plane approach requires the means to consider a noncircular cross section shape in the presence of a uniform crossflow velocity and free vortices in each plane normal to the body axis. The procedure used to handle the noncircular shapes is to determine a conformal transformation for mapping points on or outside the arbitrary body to a corresponding point on or outside a circular body. The two-dimensional potential flow solution around a circular shape in the presence of a uniform flow and external vortices is well known and has been documented numerous places in the literature.[13,14] Thus, the procedure is to obtain the potential solution for the circular body and transform it to the noncircular body. For certain limited cross section shapes like ellipses, analytic transformations are

possible, but for complex noncircular shapes, the transformation cannot be carried out analytically and a numerical transformation is required. The numerical transformation currently in use is described in detail in Ref. 15 with a brief summary presented in Refs. 2 and 6.

The sequence of events in the numerical mapping is shown in Fig. 2. The arbitrary cross section shape of the body in the σ-plane is required to have a vertical plane of symmetry. The transformation of interest will map the region on and outside the body in the σ-plane to the region on and outside a circle in the ν-plane.

The final transformation has the form

$$\sigma = -i \left[\nu + \sum_{k=0}^{K} \frac{r_o^{k+1} A_k}{\nu^k} \right] \tag{1}$$

where the A_k coefficients are obtained through an iterative scheme described in Ref. 15, and r_o is the radius of the transformed circle in the ν-plane. The derivatives of the transformation required for velocity calculations described in a later section are

$$\frac{d\sigma}{d\nu} = -i \left[1 - \sum_{k=0}^{K} \frac{r_o^{k+1} kA_k}{\nu^{k+1}} \right] \tag{2}$$

$$\frac{dv}{dx} = \frac{\left[\sum_{k=0}^{K} \frac{(k+1) r_o^k A_k}{\nu^k} \right] \frac{dr_o}{dx} + \left[\sum_{k=0}^{K} \frac{r_o^{k+1}}{\nu^k} \frac{dA_k}{dx} \right]}{- \left[1 - \sum_{k=0}^{K} \frac{r_o^{k+1} kA_k}{\nu^{k+1}} \right]} \tag{3}$$

For similar cross sections along the forebody, the second term of Eq. (3) is zero.

Body Model

A three-dimensional representation of the missile volume is needed for purposes of predicting the absolute pressure coefficient on the surface.[2] An appropriate body model for missiles with noncircular cross sections is a surface panel method similar to that described in Refs. 3 and 16; however, the use of a panel model adds significantly to the cost of each computation. For this reason, a method using discrete singularities on the body axis is selected for use with chine forebodies. The noncircular body is replaced with an equivalent axisymmetric body having the same cross sectional area distribution as the actual body. There are approximations involved with this model since the induced u-velocity due to noncircular effects is obtained from two-dimensional considerations as described later. This approach is based on high angle-of-attack slender-body theory,[17] and it has been verified with exact solutions and found to be in good agreement.[6]

The volume of the equivalent axisymmetric body is well represented by a series of point sources and sinks distributed on the axis. A number of models in varying degrees of complexity are available for this task; for example, see Refs. 18-22. For use in this analysis, the same discrete source/sink model (Ref. 21) used for the earlier work (Ref. 1) was selected for its accuracy, economy, and reliabilty. A new method described in Ref. 22 appears to have much promise in modeling axisymmetric bodies, and it should be considered as a possible improvement to the current approach.

Vortex Shedding Model

The body vortex shedding model for forebodies with chines is significantly different from the model for smooth bodies described in Refs. 1 and 2. The major difference is in the formation of the discrete vortices themselves. Since the chine is the origin of separation, it is no longer necessary to predict the separation location; however, there are other problems associated with the specification of the vortex characteristics that must be addressed.

Vortex Tracking. The equations of motion of a shed forebody vortex in the presence of other free vortices in the vicinity of a body in a uniform stream are described in Refs. 1, 2, and 6. In summary, the two equations which must be integrated along the body length to determine the trajectory of a vortex Γ_m are

$$\frac{dy_m}{dx} = \frac{v_m}{V_\infty \cos\alpha_c + u} \tag{4}$$

and

$$\frac{dz_m}{dx} = \frac{w_m}{V_\infty \cos\alpha_c + u} \tag{5}$$

where u is the axial perturbation velocity in the flow field. There are a pair of equations like (4) and (5) for each vortex in the field. As new vortices are shed, the total number of equations to solve increases by two for each added vortex. These differential equations are integrated numerically using a predictor-corrector algorithm which automatically adjusts the step size to provide a solution within a specified accuracy.

Velocity Field. The velocity components at all points in the flow field are needed for pressure calculation and vortex tracking. The procedure for determining the u,v,w-components of velocity from all singularities in the flow field is described in Refs. 1, 2, and 6.

In a crossflow plane, the complex potential in the real plane is

$$W(\sigma) = \Phi - i\Psi \tag{6}$$

and the corresponding velocity at a point "m" is

$$v_m - iw_m = \frac{dW_m(\sigma)}{d\sigma} = \frac{d}{d\nu}\left[W_m(\sigma) \right] \left| \frac{d\nu}{d\sigma} \right|_{\substack{\sigma=\sigma_m \\ \nu=\nu_m}} \tag{7}$$

The velocity components in the crossflow plane are obtained from the derivative of the complex potential as shown above. If Eq. (7) is written at a vortex location for tracking purposes, the complex potential of Γ_m is not

included in Eq. (7) to avoid the singularity at that point. The derivative of the transformation required in the above equation is obtained from Eq. (2).

It has been demonstrated with panel methods and exact potential methods that the u-velocity perturbation due to noncircular effects is important in the calculation of surface pressures and flow field velocities.[6] Since all the singularities in the flow model are two-dimensional, with the exception of the axisymmetric body volume model, it is necessary to calculate the u-velocity components from the known complex velocity potentials. The u-velocity contribution of the discrete vortices in the flow field is neglected for vortex tracking, but it is included in the surface pressure calculation.

The axial velocity, given the complex potential, is

$$u = \frac{d\Phi}{dx} = \frac{d}{dx}\left[\text{Real}(W)\right] = \text{Real}\left[\frac{dW}{dx}\right] \qquad (8)$$

From the various components of the complex potential, the noncircular contributions to Eq. (8) are

Crossflow due to α:

$$\frac{dW_1}{dx} = -i\, V_\infty \sin\alpha \frac{dv}{dx} \qquad (9)$$

Crossflow due to β:

$$\frac{dW_2}{dx} = -V_\infty \sin\beta \frac{dv}{dx} \qquad (10)$$

Cylinder in α flow (two-dimensional doublet:

$$\frac{dW_3}{dx} = i\, V_\infty \sin\alpha \left[\frac{2v r_o \frac{dr_o}{dx} - r_o^2 \frac{dv}{dx}}{v^2}\right] \qquad (11)$$

Cylinder in β flow (two-dimensional doublet):

$$\frac{dW_4}{dx} = V_\infty \sin\beta \left[\frac{2v r_o \frac{dr_o}{dx} - r_o^2 \frac{dv}{dx}}{v^2}\right] \qquad (12)$$

where dv/dx is available from the transformation in Eq. (3).

Since the axisymmetric body source singularities are three-dimensional, they contribute an induced axial velocity. However, as noted previously, these axial velocities are axisymmetric, and they exhibit no direct effect of the noncircular shape. This deficiency can be corrected using the techniques of high angle-of-attack slender-body theory.[17] An approximation to the perturbation u-velocity due to the growing noncircular shape is obtained as follows.

The equivalence rule, described in Section 6-4 of Ref. 23 and expanded for application to this problem in Ref. 17, states that [1] the flow far away from a general slender body becomes axisymmetric and equal to the flow around an equivalent axisymmetric body, and [2] near the slender general body, the flow is different from that around the equivalent axisymmetric body by a two-dimensional component that is required to satisfy the tangency boundary condition. Or, the difference between the velocity potential for the noncircular body and that for the equivalent body of revolution is equal to the increment of the velocity potential due to the noncircular effect. Thus,

$$\Phi_n - \Phi_{eq} = \Phi_{\Delta n} \qquad (13)$$

For purposes of including the effect of the noncircular body on the u-velocity, the following analysis is included. The velocity potential for an expanding cylinder in the crossflow plane, represented by a two-dimensional source singularity, is

$$W_7(\sigma) = r_{eq} \frac{dr_{eq}}{dx} \ln v\, V_\infty \cos\alpha \qquad (14)$$

Applying Eq. (8) to Eq. (14) for both terms on the left side of Eq. (13), remembering that $dv/dx=0$ for circular cross sections, the contribution due to the growing noncircular forebody becomes

$$\left.\frac{dW_7}{dx}\right|_{\Delta n} = V_\infty \cos\alpha \left[\frac{r_{eq}}{v} \frac{dr_{eq}}{dx} \frac{dv}{dx}\right] \qquad (15)$$

This velocity represents the increment in the u-velocity caused by the noncircular shape of the body.

Finally, the u-velocity in the flow field of a noncircular body is calculated by including Eqs. (9) through (12) and (15) in Eq. (8). This result is combined with the axial velocity from the three-dimensional source/sink model to obtain the total u-velocity on the body surface and in the flow field. This approach, though slightly different from that presented in Ref. 17, produces results that are in excellent agreement with high angle-of-attack slender-body theory when applied to ellipsoid bodies.

Surface pressure distribution.- The surface pressure distribution on the forebody is used to calculate forces and moments. The surface pressure coefficient is determined from the Bernoulli equation in the form

$$C_p = \frac{2}{\gamma M_\infty^2}\left\{\left[1 + \frac{\gamma-1}{2} M_\infty^2 (C_{p_I})\right]^{\frac{\gamma}{\gamma-1}} - 1\right\} \qquad (16)$$

where

$$C_{p_I} = 1 - \left[\frac{U}{V_\infty}\right]^2 - \frac{2\cos\alpha_c}{V_\infty}\frac{d\Phi}{dx} \qquad (17)$$

U is the total velocity (including V_∞) at a point on the body. The last term in Eq. (17) represents the axial velocity contribution from the two-dimensional shed vortices in the flow model. Details of the calculation of this important term are presented in Ref. 6.

Separated wake.-The separated wake on the lee side of the body is represented by a large number of discrete vortices, each vortex originating on the chine edge at each axial marching step in the calculation. The major portion of

the lee side vortex wake has its origin at the chine edge, but a portion of the wake originates from the secondary separation points located in the reverse flow region on the lee side of the body. Secondary separation is not included in the calculations for this paper.

For smooth bodies,[1,2] the separation causing the vortex shedding into the lee-side wake is of a type traditionally associated with boundary layer separation. The strength of the vortex is determined by the vorticity in the boundary layer, and the initial position of the shed vortex is determined such that the surface velocity in the crossflow plane at the separation point is exactly canceled by the shed vortex and its image.

For bodies with chines or other sharp edges, the primary separation location is fixed at the sharp edge, thus negating the need to predict the separation location on the body. The appropriate boundary condition is to assume the flow leaves the sharp edge smoothly; that is, the Kutta condition is satisfied at the edge. This boundary condition transforms to a stagnation point in the circle plane at the separation point.

The common difficulty for all vortex cloud methods applied to sharp edges (e.g., Refs. 5, 7, and 10), including the present method (Ref. 6), lies in the solution for the shed vortex at each time step. Only one equation is available from the Kutta condition to solve for two unknowns, the vortex strength and its position. In the smooth body analysis, an external boundary condition provides the missing equation. This condition is the determination of the strength of the vortex from the vorticity in the boundary layer prior to separation. In some methods noted above, the analysis was developed for delta wings, and the assumption of conical flow provided the necessary information. A slightly different approach was selected for the present work.

The initial approach is based on the method developed by Sacks.[10] At the first shedding station on the forebody and chine, there is no vorticity in the field; therefore, the chine edge is a singularity and it is not possible to calculate a realistic v-velocity near the sharp edge. Thus, the solution is started by assuming the velocity outboard at the chine edge is approximately represented by $v = 0.5\sin\alpha$, and the shed vortex is convected outboard a distance $v\Delta t$, where Δt is defined as $\Delta x/V_\infty\cos\alpha$. With the position of the vortex determined in this manner, the strength is obtained from the Kutta condition at the sharp edge.

In the current model, the pressure distribution is calculated at the initial station with no vorticity in the field; therefore, there is a singularity at the chine edge. The average tangential velocity over the outer 10-percent of the chine, excluding the singularity, is used to locate the initial shed vortex. This initial vortex position satisfies the requirement for one of the two equations, and the remaining equation can be used to calculate the strength of the vortex such that the Kutta condition at the chine edge is satisfied. With a vortex in the field which satisfies the Kutta condition, it can be convected with the local flow field during the next axial marching step. Now, though the Kutta condition is not satisfied after the vortex moves, the tangential velocity can be calculated at several points on the forebody near the chine edge. The velocities on the outer ten percent of the chine semispan are averaged to find a convecting velocity for the next shed vortex. As before, when the position is known it is possible to determine the strength by satisfying the Kutta condition at the chine edge.

The method of convecting the shed vortex to its initial position has been the subject of much discussion between investigators, and there are nearly as many methods as there are investigators. When a sheet of vorticity is shed from the trailing edge of an airfoil in unsteady motion, a case is made in Ref. 24 that the sheet should leave the edge tangent to the surface. In Ref. 25, another procedure for locating the shed vortex next to the edge of a cambered plate is described. Several alternative methods are described in Ref. 6. In the analysis described herein, the shed vortex is convected to its initial position along a line tangent to the windward surface of the chine.

Vortex core. - The diffusion core model for the point vortex-induced velocities removes the singularity at the vortex origin and effectively reduces the velocities near the vortex.[2] A number of core models have received considerable attention in the context of body vortex-induced effects, and use of these models has a number of shortcomings; however, the practical aspects of tracking vorticity and calculating discrete vortex effects on bodies dictate that some kind of core model is essential. In the current model, the radial location of the maximum induced velocity is fixed at a specific radius.

Vortex Tracking Calculation

Calculation of the motion of the discrete vortices after they are shed from the body is a key component of the prediction method. The location of the vortices and the cloud formed influences the strength and subsequent positions of later vortices shed from the body, and ultimately, the tracked positions of the vortices determines the induced loading on the body. As noted by other investigators,[25] it is common for tracking problems to arise during the normal calculation of the motion of the individual vortices. The usual nature of these problems is a vortex inside the body, and the usual solution is to simply eliminate the offending vortex from the flow field.

In the current model,[6] the solution is to replace the vortex back into the flow field outside the body and allow it to continue as part of the cloud. This procedure has been reasonably successful on axisymmetric bodies, though the problem occurs so infrequently in most configurations examined by the authors that it is difficult to test the validity of this approximate solution. Initially, this procedure did not prove very successful for the analysis of chine configurations; therefore, some work was directed at understanding the mechanics of the tracking problem in the anticipation that it could be eliminated.

The equations of motion of the vortices are shown in Eqs. (4) and (5). The motion of a vortex is determined by integrating these equations, along with those for the other vortices, from one axial station to the next, a distance Δx. For most purposes, Δx is a constant over the entire length of the body; although, as discussed in Ref. 3, Δx can be a variable length. When the tracking procedure was originally developed, the u-velocity in the denominator of Eqs. (4) and (5) was included to correct for the effect of a growing body near the nose. For axisymmetric bodies, the u-velocity was determined by the three-dimensional source singularities representing the body. This velocity was essential for the

successful tracking of vortices shed near the nose, and, upon a brief analysis, it becomes obvious why this is the case. Eqs. (4) and (5) represent to first order the slope of the vortex filament between the two axial stations. If a vortex is very near the body surface, the slope must be the same as the body slope or greater, or the vortex will be tracked inside the body; therefore, near the body nose the u-velocity from the sources (which is opposite in sign from $V_\infty \cos\alpha_c$) is necessary to decrease the magnitude of the denominator and increase the slope of the filament, thus keeping the vortex from penetrating the body surface during tracking.

For noncircular bodies, the effect of the body shape on the v- and w-velocities in Eqs. (4) and (5) is included by means of the conformal transformations. In the original work,[1,2] the u-velocity was included as an axisymmetric effect from the equivalent body, and there was no noncircular effect on the u-velocity. In the extension of the original analysis reported in Ref. 6, the approximate contribution of the noncircular shape to the u-velocity is determined from Equation (8). When the full u-velocity is included in the tracking, the vortices track inside the body on a regular basis. The difficulty appears to be a subtle violation of one of the basic assumptions inherent in the vortex cloud procedure.

Under the unsteady flow analogy approximation, vortex tracking in the axial direction assumes that all the vortices are moving at the same u-velocity such that they traverse the Δx-distance between axial stations in the same time. When the u-velocity consists of a free-stream component and a volume or source component, this assumption is nearly correct for all vortices near the body, even when the body is noncircular and there is a variation in u-velocity around the body. However, when the doublet effects are included, the u-velocity can vary significantly around the body and with distance from the body. In this case, the vortices are not all traversing axially at nearly the same velocity, and the unsteady analogy approximation is incorrect. The numerical problems can be explained using Eqs. (4) and (5). On the lee side of the body, the doublet singularities represent the acceleration of the u-velocity on that side of the body, the denominator becomes very large near the body, and the slope of the vortex filament decreases until it can be less than the slope of the body. As a consequence, the vortex tracking calculation may force the vortices inside the body.

For purposes of the current prediction method, the u-velocity used for tracking purposes does not include the doublet terms; however, these terms are included in the surface pressure and velocity field calculation.

RESULTS

Comparison of measured and predicted aerodynamic characteristics on typical forebodies with chines is the most reliable means to evaluate the strengths and weaknesses of the engineering method. Since pressure distributions provide the best assessment of the capabilities of a prediction method, the configuration and experimental data of Ref. 26 provide a wide range of information for verification of the method. The forebody model with the three specific axial stations at which pressures are measured is shown in Fig. 4. The experimental data shown in the following figures were measured with a 60-degree delta wing in place aft of the forebody, but it appears that the wing had a minimal influence at all but the last pressure station on the body. The effect of the wing is not modeled in the prediction method.

Measured and predicted pressure coefficients on the upper surface of the forebody are shown in Fig. 5 for the configuration at $\alpha = 10°$. Though data are not available, predicted pressures on the lower surface are shown in these figures. The predicted vortex cloud pattern at each station is shown to provide some perspective on the region of influence of the lee side vortex. In Fig. 5(a), the measured and predicted pressure coefficients at the first forebody station, x = 7 inches from the nose, are compared. The predicted pressures have the correct characteristics on the suction side of the body, but the suction peak caused by the vortex seems to be spread over a larger region than that measured. The pressure on the lower surface is nearly constant. The predicted pressure distribution without vortex effects is shown as a dashed curve. At this low angle of attack, the vortex-induced effects are confined to the upper surface of the chine.

In Fig. 5(b), the second axial station exhibits lower suction pressures on the upper surface, and the predicted results are in very good agreement with experiment except for the suction peak near the chine edge. The last axial station at x = 20 inches in Fig. 5(c) shows good agreement between the measured and predicted pressure distributions on the upper surface. The vortex-induced effects are less at this station than at the previous station even though the vortex strength has increased. This is caused by the increased distance between the rolled-up vortex and the chine upper surface. At the aft station, the rolled-up vortex is displaced outboard and upward from the chine edge, thus decreasing the vortex-induced pressure.

Measured and predicted results on the same configuration at $\alpha = 20°$ are presented in Fig. 6 for the same three axial stations. The predicted pressure distribution on the forebody without separation is shown as the dashed curve to illustrate the induced effects of the vortices. As expected from the vortex fields, the influence of the chine vortex is concentrated on the chine and the region of the chine-body junction.

In general, the results at $\alpha = 20°$ with separation effects included are the same as shown in the previous figures for the first two axial stations. The agreement between measured and predicted pressures is very good. At the aft axial station, the predicted suction pressure on the lee side is significantly lower than that measured. The explanation is not obvious at this time, but the problem could be with the predicted strength and/or position of the shed vortex, or it could be due to some external influence such as the wing. There is not sufficient experimental data available to assess the effect of the wing; however, the presence of a lifting wing could contribute to lower pressures on the forebody in the vicinity of the wing.

When the angle of attack is increased to 30 and 40 degrees in Figs. 7 and 8, respectively, the results become very consistent at all stations on the forebody. The predicted pressure distribution is in good agreement with the measurements on the fuselage upper surface away from the chine, but the agreement is generally poor everywhere on the chine. The predicted suction pressure is always less than that measured; therefore, the integrated normal force will be less than that measured at the higher angles of attack. The

problem on the chine could be caused by the vortex position. It is apparent from the vortex fields shown on each figure that as the angle of attack increases, the vortex moves farther from the body thus reducing its effect. Comparison of the predicted pressures with and without the vortex field show that the method does represent the qualitative effects of the vorticity even though the actual pressure levels are not in good agreement with experiment.

It is possible that secondary separation on the lee side of the forebody can be changing the vorticity distribution in the flow field sufficiently to have a measurable effect on the pressure distribution. Secondary separation effects were not included in these calculations.

When the forebody at angle of attack is yawed to some nonzero sideslip flow angle, the separation becomes asymmetric. The assumption is made that separation still occurs at the chine on both sides of the forebody, but the asymmetric flow field changes the tracking and subsequent vortex distributions. This assumption is good for moderate yaw angles, but when the yaw angle approaches the angle of attack, the flow is approaching the windward chine at a low incidence angle, and separation may occur on the body surface rather than at the chine edge. It is possible in such a flow condition for multiple separation points to exist, but the present method will not permit separation at a location away from the chine edge.

In Figs. 9 and 10, comparisons of measured and predicted pressure distributions are shown for the forebody at $\beta = 10°$ and $\alpha = 20°$ and $30°$, respectively. The agreement at the first axial station is only fair on the chines at both angles of attack, and it is clear that the vortices are not having enough influence on the local pressures on the downwind chine. Some of the difficulties with these results can be explained by studying the vortex field, also shown in the figures. At the first station, the vortex on the right side of the body seems to be spread out over a large region of the lee side of the body, and the influence of the vortex on the surface pressure reflects this phenomenon. The predicted vortex induces a low pressure over more of the upper surface than is measured, but the pressure peak near the chine edge for $\alpha = 30°$ is lower than indicated by the experiment. As for the $\beta = 0°$ flow condition described above, the pressure level at the lower angle of attack is in better agreement with the measured pressures. On the left side of the body the vortex is rolled up in a loose fashion and is concentrated away from the body surface. As a consequence, the predicted suction pressure peak is significantly lower than that measured.

At the second axial station shown in Figs. 9(b) and 10(b), the vortex on the right side is much stronger than at the previous station; it is tightly rolled up, and, as a consequence, the suction peak is in better agreement with experiment. The vortex on the left side is also tightly rolled up, but it is concentrated away from the body, and its influence on the pressure distribution is less than that measured at the higher angle.

Finally, at the third axial station shown in Figs. 9(c) and 10(c), the vortex is tightly rolled up near the body, and the predicted pressure peak on the chine is in good agreement with experiment. Though the left chine vortex is rolled up a large distance from the chine surface, the pressure levels are in reasonable agreement with the measurements except for a small region on the body near the junction with the chine.

The discrete vortex fields shown in the above pressure figures help illustrate the extent of the vorticity shed from the chine, but these results do not provide much information on the nature of the physics of the flow in the vicinity of the forebody. To better understand the full effect of the shed vorticity, flow field calculations provide a direct visualization of the velocity field. A representative set of velocity vectors in the flow field adjacent to the forebody at $\alpha = 20°$ is shown in Fig. 11. The accuracy of the flow vectors inside the vortex or very near individual vortices will be in question because of the influence of the discrete vortices, but the overall character of the flow field is correct. These vector plots are most useful in visualizing the region of influence of the vortex, particularly if there is concern about vortex-induced loads on other components of the airframe.

To illustrate the effect of angle of attack on the shed vortex strength near a forebody with a chine, the predicted vortex strength as a function of angle of attack and distance along the forebody is shown in Fig. 12.

CONCLUSIONS

An engineering prediction method based on a rational flow modeling technique to predict the vortex shedding from forebodies with chines in subsonic flow at angles of attack and roll is described. Comparisons of measured and predicted aerodynamic characteristics and flow field quantities are used to verify the flow model and prediction method for a chine forebody configuration under a wide range of flow conditions. The method has proved successful in representing the principal features of the complex flow field on the lee side of these configurations at moderate angles of attack; therefore, it has application as an engineering or preliminary design technique directed at the prediction of nonlinear aerodynamic characteristics resulting from high angle of attack flows.

The prediction method described herein has further application as one component of a larger prediction method for complete configurations consisting of an arbitrary body and multiple fins. The ability to model the correct flow field in the vicinity of the body leads to the capability to calculate body separation wake-induced interference effects on fins and other control surfaces. The vortex shedding analysis and prediction techniques are also applicable for use in other codes; for example, the methods developed in this investigation can be transferred to higher order codes such as panel codes.

ACKNOWLEDGEMENTS

This work was supported in part by the NASA/Langley Research Center under Contract NAS1-17077 and by NEAR under an IR&D program. The authors are grateful to Dr. Robert M. Hall of the NASA/Langley Research Center and Dr. Michael J. Hemsch of Lockheed Engineering & Sciences Co. for their constructive comments and able assistance throughout the course of this investigation.

REFERENCES

1. Mendenhall, M. R. and Lesieutre, D. J.: Prediction of Vortex Shedding From Circular and Noncircular Bodies in Subsonic Flow. NASA CR-4037, January 1987.

2. Mendenhall, M. R. and Perkins, S. C., Jr.: Vortex Cloud Model for Body Vortex Shedding and Tracking. Tactical Missile Aerodynamics, Vol. 104 of Progress in Astronautics and Aeronautics, ed. by M. J. Hemsch and J. N. Nielsen, AIAA, 1986.

3. Mendenhall, M. R. and Perkins, S. C., Jr.: Prediction of Vortex Shedding From Circular and Noncircular Bodies in Supersonic Flow. NASA CR-3754, January 1984.

4. Marshall, F. J. and Deffenbaugh, F. D.: Separated Flow Over Bodies of Revolution Using an Unsteady Discrete-Vorticity Cross Wake. NASA CR-2414, June 1974.

5. Sarpkaya, T.: Computational Methods With Vortices - The 1988 Freeman Scholar Lecture. ASME J. Fluids Engineering, March 1989, Vol. 111, pp. 5-52.

6. Mendenhall, M. R. and Lesieutre, D. J.: Prediction of Subsonic Vortex Shedding From Forebodies with Chines. NEAR TR 391, December 1989.

7. Oh, S., Tavella, D., and Roberts, L.: Theoretical Studies on Flapped Delta Wings. JIAA TR-85, Stanford University, August 1988.

8. Brown, C. E. and Michael, W. H., Jr.: On Slender Delta Wings with Leading-Edge Separation. NACA TN 3430, 1955.

9. Mangler, K. W. and Smith, J. H. B.: Calculation of the Flow Past Slender Delta Wings with Leading-Edge Separation. RAE Report No. Aero. 2593, May 1957.

10. Sacks, A. H., Lundberg, R. E., and Hanson, C. W.: A Theoretical Investigation of the Aerodynamics of Slender Wing-Body Combinations Exhibiting Leading-Edge Separation. NASA CR-719, March 1967.

11. Hoeijimakers, H. W. M. and Bennekers, B.: A Computational Model for the Calculation of the Flow about Wings with Leading-Edge Separation. AGARD CP-247, 1972.

12. Kandil, O. A.: Computational Technique for Compressible Vortex Flows Past Wings at Large Incidence. J. of Aircraft, Vol. 22, No. 9, 1985, pp. 750-755.

13. Mendenhall, M. R. and Nielsen, J. N.: Effect of Symmetrical Vortex Shedding on the Longitudinal Aerodynamic Characteristics of Wing-Body-Tail Combinations. NASA CR-2473, January 1975.

14. Nielsen, J. N.: Missile Aerodynamics. Nielsen Engineering & Research, Inc., 1988.

15. Skulsky, R. S.: A Conformal Mapping Method to Predict Low-Speed Aerodynamic Characteristics of Arbitrary Slender Re-Entry Shapes. J. of Spacecraft, Vol. 3, No. 2., February 1966, pp. 247-253.

16. Lesieutre, D. J., Mendenhall, M. R., and Torres, T. O.: Missile Stability and Methods Development, Vol. III - Programs SUBVTX and SUPVTX for Determining Aerodynamic Characteristics of Arbitrary Missile Bodies Including Separation Vorticity. NEAR TR 396, August 1989.

17. Hemsch, M. J.: Comparison of High Angle-of-Attack Slender-Body Theory and Exact Solutions for Potential Flow Over an Ellipsoid. To be published in J. Aircraft.

18. Wolfe, W. P. and Oberkampf, W. L.: A Design Method for the Flow Field and Drag of Bodies of Revolution in Incompressible Flow. AIAA Paper 82-1359, August 1982.

19. Janikowsky, L. C. and Sarpkaya, T.: Optimized Discrete-Singularity Representation of Axisymmetric Bodies. AIAA Paper 85-0284, January 1985.

20. Christopher, P. A. T.: The Generation of Axi-Symmetric Bodies in Incompressible Flow by Means of Distributions of Complex Sources. Cranfield Report CoA 8304, March 1983.

21. Goodwin, F. K., Nielsen, J. N., and Dillenius, M. F. E.: A Method for Predicting Three-Degree-of-Freedom Store Separation Trajectories at Speeds up to the Critical Speed. AFFDL-TR-71-81, July 1971.

22. Hemsch, M. J.: An Improved, Robust, Axial Line Singularity Method for Bodies of Revolution. AIAA Paper 89-2176, July 1989.

23. Ashley, H. and Landhal, M.: Aerodynamics of Wings and Bodies. Addison-Wesley Pub. Co., Inc., 1965.

24. Giesing, J. P.: Vorticity and Kutta Condition for Unsteady Multienergy Flows. ASME J. Applied Mech., September 1969, pp. 608-613.

25. Mostafa, S. I. M.: Numerical Simulation of Unsteady Separated Flows. Ph.D. Thesis, Naval Postgraduate School, Monterey, CA, June 1987.

26. Erickson, G. E. and Brandon, J. M.: Low-Speed Experimental Study of the Vortex Flow Effects of a Fighter Forebody Having Unconventional Cross-Section. AIAA Paper 85-1798, August 1985.

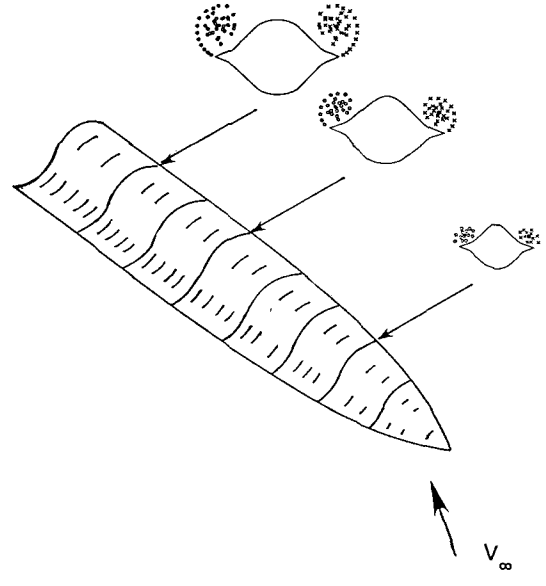

Figure 1. - Lee side vortex formation on a forebody with chine.

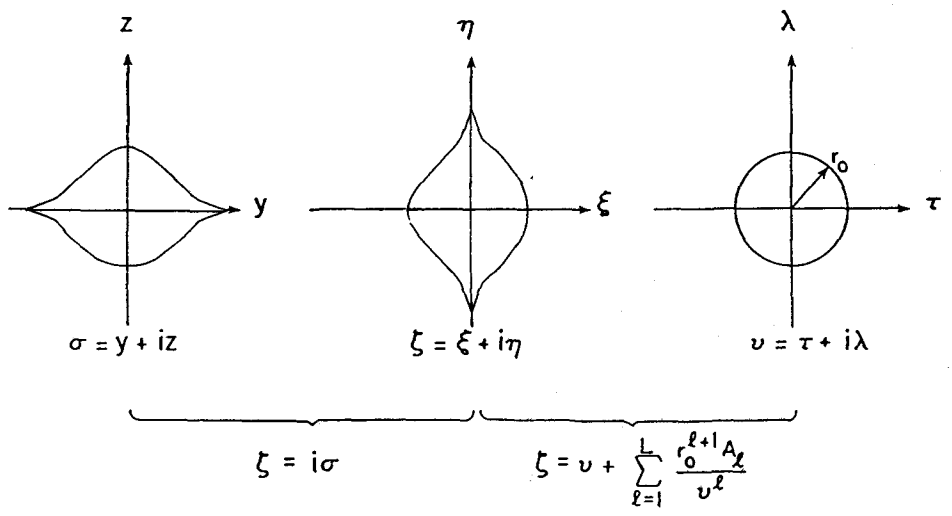

Figure 2. - Conformal mapping nomenclature.

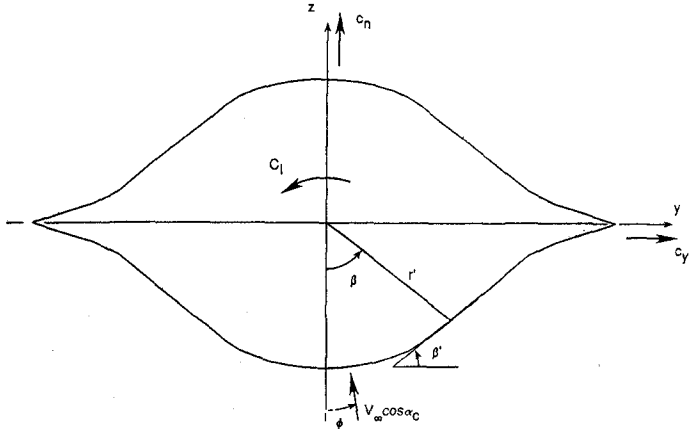

Figure 3. - Forebody cross section nomenclature.

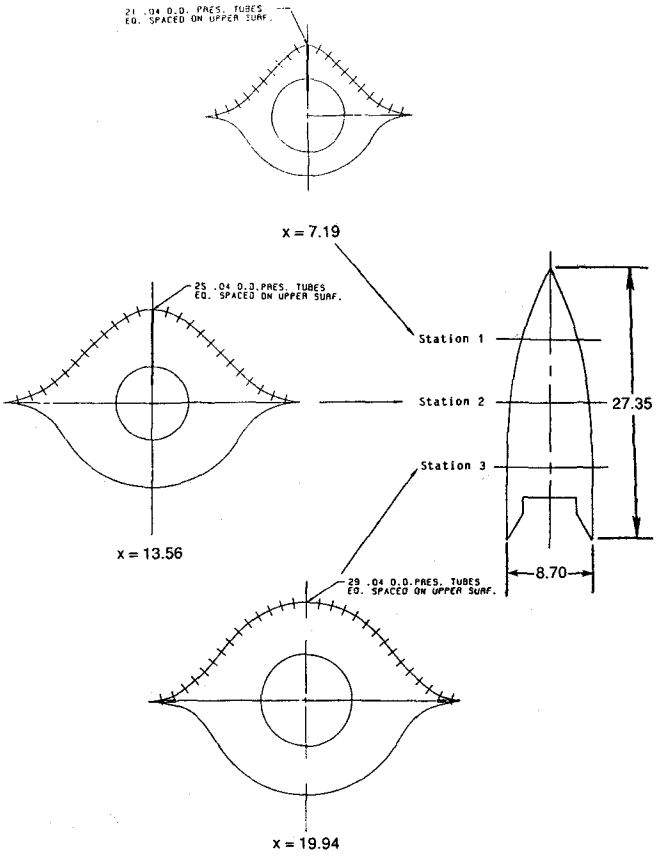

Figure 4. - Forebody with chine details, Ref. 26.

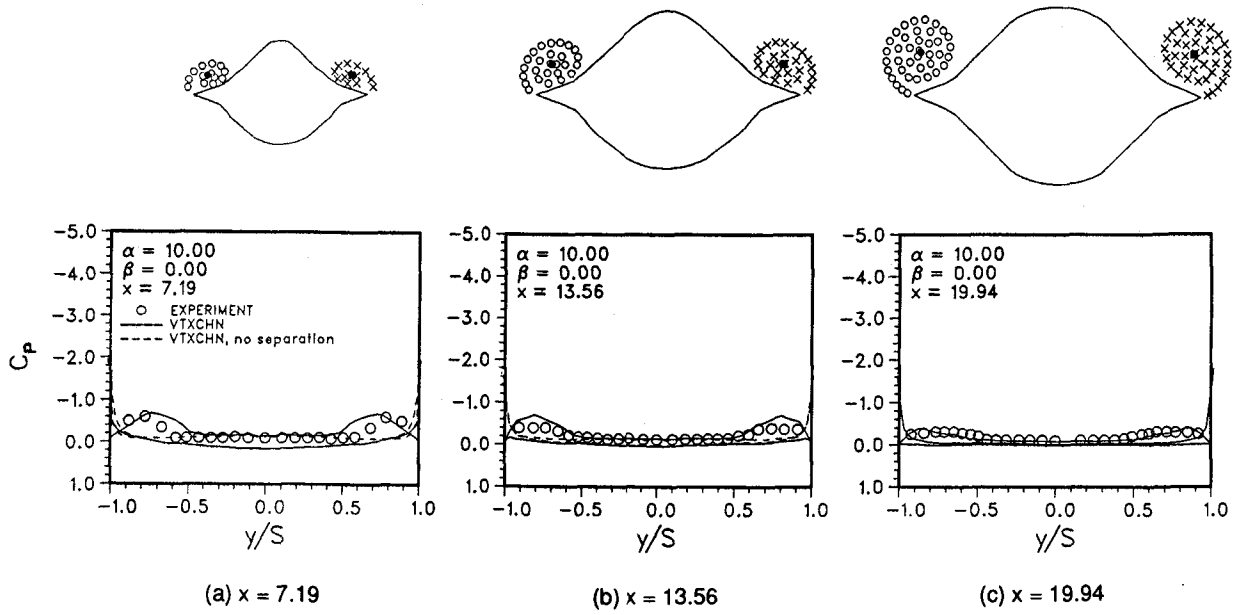

Figure 5. - Measured and predicted pressure distributions on a forebody with chine, $\alpha = 10°$.

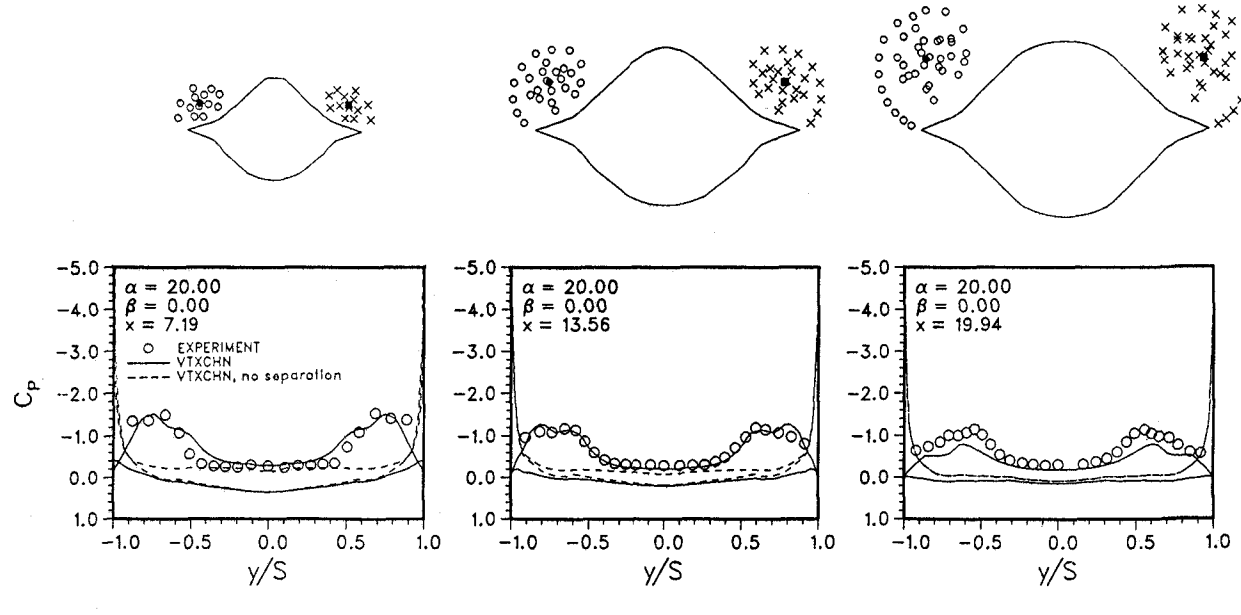

Figure 6. - Measured and predicted pressure distributions on a forebody with chine, $\alpha = 20°$.

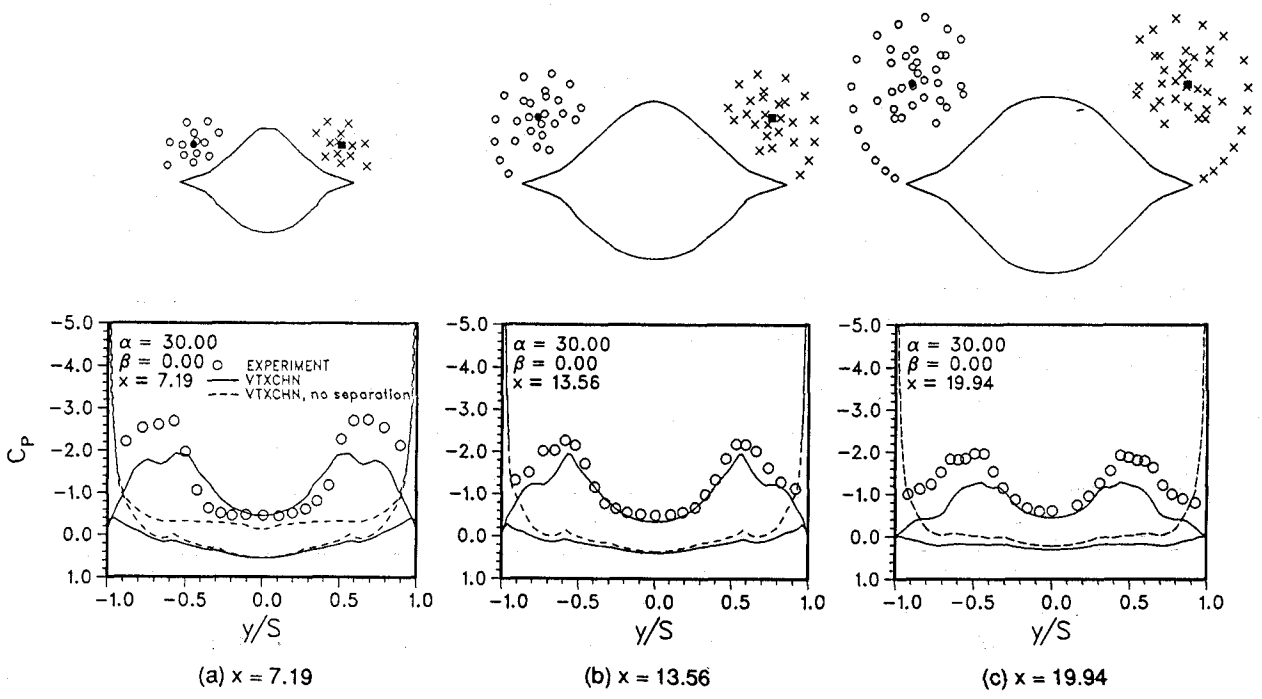

Figure 7. - Measured and predicted pressure distributions on a forebody with chine, $\alpha = 30°$.

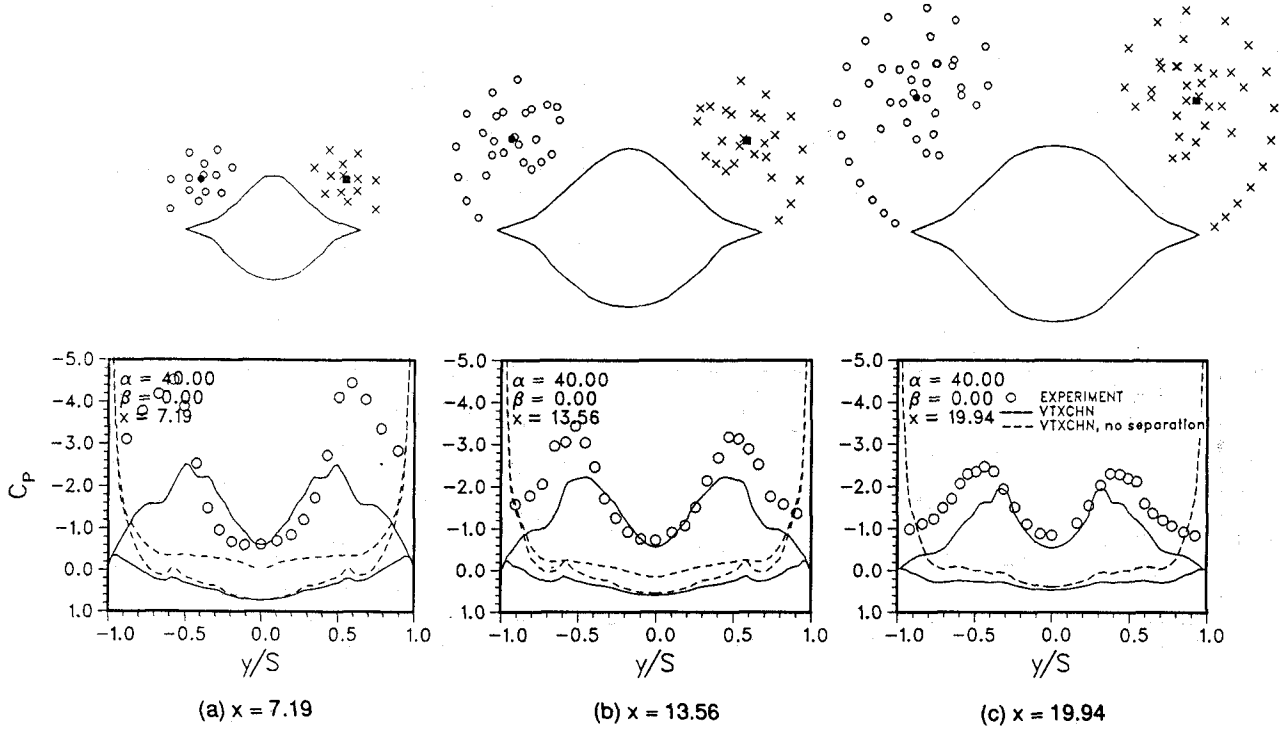

Figure 8. - Measured and predicted pressure distributions on a forebody with chine, $\alpha = 40°$.

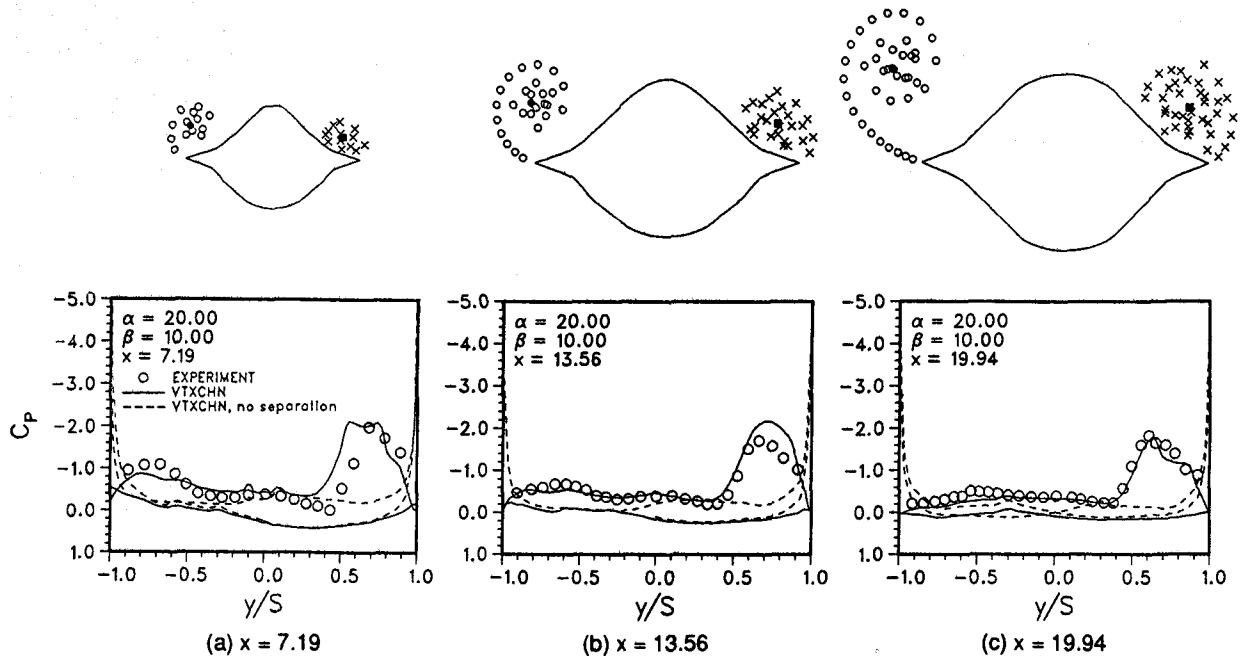

Figure 9. - Measured and predicted pressure distributions on a forebody with chine, $\alpha = 20°$, $\beta = 10°$.

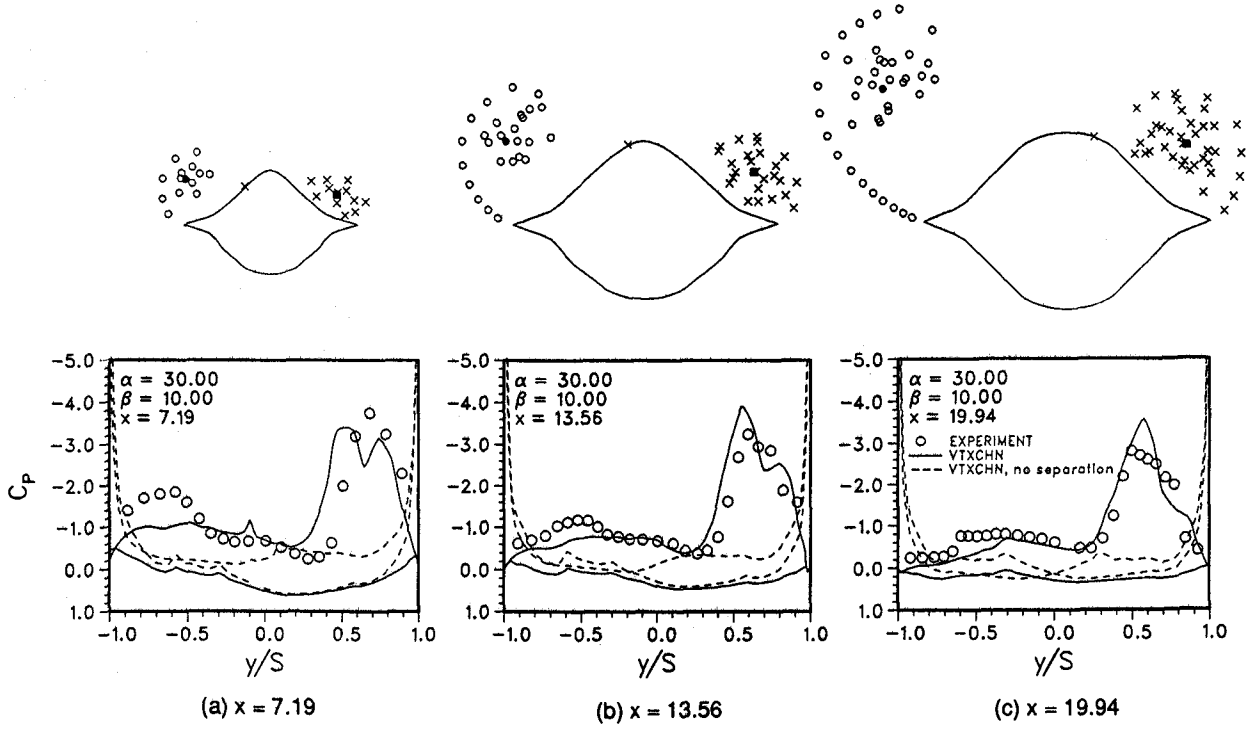

Figure 10.- Measured and predicted pressure distributions on a forebody with chine, $\alpha = 30°$, $\beta = 10°$.

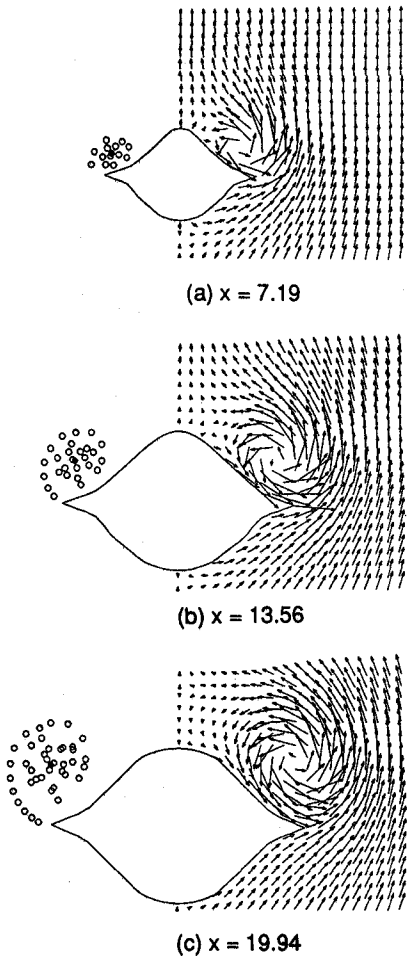

Figure 11.- Predicted velocity vectors near a forebody with chine, $\alpha = 20°$.

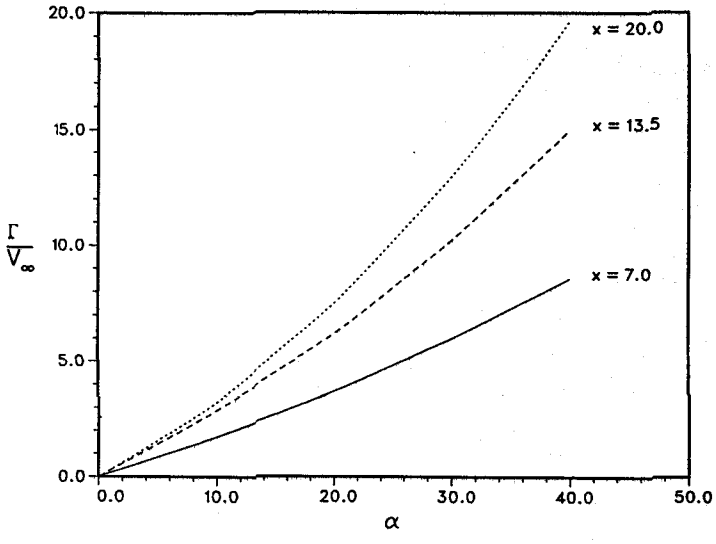

Figure 12.- Predicted vortex strength near a forebody with chine.